

Analysis of the Phase Transition during High Speed Scratching of Silicon

Ariely Miranda Dias

Bachelor Thesis
December 2021

Stefan Süssmaier
Prof. Konrad Wegener

Abstract

When cutting brittle materials at small scales, machining in ductile regime can be obtained. Increasing the depth of cut to a critical value leads to a ductile to brittle transition in the removal process. The ductile machining is associated with phase transitions. This study investigated the change in the phase transitions when machining monocrystalline silicon with a diamond indenter. The experimental setup kinematic was that of a face turning process with no overlapping trace, with Vickers and Berkovich indenters in different orientations. The analysis of phases was performed in Raman microspectroscopy. The scratches provided evidence that even the material removal mechanism being different for the different indenters and orientations, this change does not have a significant influence on the Raman intensity ratio of amorphous phase against crystalline phase. For the diamond wire sawing process, this means that the grain shape of diamonds in the wire will not influence the surface residual phases.

Resumo

Ao cortar materiais frágeis em pequena escala, é possível obter usinagem em regime dúctil. O aumento da profundidade de corte até um valor crítico leva a uma transição dúctil-frágil no processo de remoção. A usinagem em regime dúctil está associada a transições de fase. Este estudo investigou a mudança nas transições de fase ao usinar silício monocristalino com um indentador diamantado. Experimentos de riscos ("*scratching*") foram realizados em silício monocristalino. A cinemática dos experimentos foi a de um processo de torneamento facial sem traços sobrepostos, com indentadores Vickers e Berkovich em diferentes orientações. A análise das fases foi realizada em microspectroscopia Raman. Os riscos forneceram provas de que mesmo o mecanismo de remoção de material sendo diferente para os diferentes indentadores e orientações, esta alteração não tem influência significativa na relação de intensidade da fase amorfa Raman contra a fase cristalina. Para o processo de corte com fio diamantado, isto significa que a forma do grão dos diamantes no fio - ainda afiados - não influenciará as fases residuais da superfície.

Acknowledgment

First of all, I would like to thank the professors Konrad Wegener and Fábio Antonio Xavier and the Process Group Leader, Michal Kuffa, for the opportunity of undertaking an internship at the Institute of Machine Tools and Manufacturing, IWF and writing my bachelor thesis.

Next, I would like to thank Stefan Süssmaier for the guidance and assistance and for the productive discussions that contributed a lot to the development of this research.

I also thank my co-workers, especially Paulo, Lucas, Martina, Joy and Christian for providing a laid-back and happy atmosphere at the institute, which makes it an excellent workplace.

Furthermore, I would like to express gratitude to the professionals of Universidade Federal de Santa Catarina for the dedication they have to the undergraduate course of materials engineering and to the internships, providing the students great professional experiences.

Finally, I would like to thank my family, my boyfriend and my friends for the incentive and unconditional support they provide me, especially during this new phase I have been living.

Contents

List of Figures	x
List of Tables	xi
List of Abbreviations	xiii
List of Symbols	xv
1 Introduction	1
1.1 Motivation	1
1.2 Related Work	1
1.3 Overview	2
2 Literature review	3
2.1 Monocrystalline silicon and wafers	3
2.2 Silicon wafers machining	4
2.2.1 Loose abrasive and diamond wire sawing	5
2.2.2 Phase transitions	6
2.2.3 Raman spectroscopy	8
2.2.4 Scratching tests	10
3 Reseach gap	15
4 Materials and methods	17
4.1 Silicon workpiece	17
4.2 Cutting tool and experimental setup	17
4.3 Measurement instruments	19
4.4 Experimental plan	20

5	Results and Discussion	21
5.1	Scratch profiles	21
5.1.1	Residual cutting depth	21
5.1.2	Phase transition and intensity ratio	23
6	Conclusion and Future Work	29
6.1	Conclusion	29
6.2	Future Work	30
A	Appendix	31
A.1	Scratches profiles	31
A.2	Groove center Raman overview	32
	Bibliography	35

List of Figures

2.1	(a) Crystalline structure of silicon in the projections tree-dimensional and bi-dimensional [8] and (b) Crystallographic planes of monocrystalline silicon [9]	3
2.2	Schematic of critical depth of cut identification. Extracted from [16]	4
2.3	(a) Loose abrasive slurry sawing (extracted from [1] and (b) diamond wire sawing	5
2.4	Material removal mechanisms in (a) Loose abrasive (extracted from [1] and (b) diamond wire sawing of silicon	6
2.5	Schematic of the phase transformations cycle in silicon under contact loading [20]	7
2.6	Wafer warp due to residual stress and surface damage [26]	8
2.7	Typical information of Raman spectra and corresponding material information [30]	9
2.8	Raman spectra showing (a) only crystalline peak and (b) amorphous peak [31]	9
2.9	Curve fitting method for separating Raman peaks (a) comparison of experimental Raman spectra and fitted curve; (b) separated Raman peaks of amorphous and crystalline silicon [31]	10
2.10	Simulation of the number of particles on wire in contact with the crystal surface due to size distribution [5]	11
2.11	Optical micrographs of scratches with different material removal from different tools. Extracted from [32].	11
2.12	Raman spectra of different positions within the scratched grooves made at (a) 1 mm/min, (b) 1 mm/min with a smaller scale of Raman spectra intensity than Fig. a, (c) 10 m/s and (d) 20 m/s (the 0–800 nm in all legends indicates the distance from the scratch centerline). Extracted from [34]	12
2.13	3D AFM images of scratches (a) edge-on orientation of scratching (E-scratching) and (b) face-on orientation of scratching (F-scratching). Extracted from [36]	13
4.1	Silicon workpiece used for the experiments; the scratches can be seen on the surface as thin white lines	18
4.2	Sensofar Microscope images of (a) Vickers (b) Berkovich and (c) Rockwell indenters with 150x magnification	18

List of Figures

4.3	Experiments setup: diamond indenter attached fixed to the force measurement platform under the silicon workpiece attached to the spindle	19
4.4	The scheme of the Berkovich and Vickers orientation relative to the direction of scratching. Adapted from [20]	19
5.1	Overview and profile of Vickers (a) 0 and (b) 45 degrees	22
5.2	Raman analysis of (a) Berkovich 180° and (b) Vickers 45°	23
5.3	Curve fitting method (a) comparison of original experimental Raman data and fitted curve; (b) separated Raman peaks of amorphous and crystalline silicon	24
5.4	(a) Overview Berkovich 0 scratch spectrums - each color represents measurements at the one different cutting depth. Zoom in for experiments represented in blue color in (b) Overview scratch Berkovich 0 for cutting depth = 0.8 - absence of Si-IV peaks	25
5.5	Intensity ratio vs cutting depth for all scratch experiments	26
A.1	Overview and profile of Vickers (a) 0 and (b) 45 degrees scratches	31
A.2	Overview and profile of Berkovich (a) 0 and (b) 180 degrees scratches	32
A.3	Raman data analysis overview for berkovich edge-on scratches	33
A.4	Raman data analysis overview for berkovich face-on scratches	33
A.5	Raman data analysis overview for vickers edge-on scratches	34
A.6	Raman data analysis overview for vickers face-on scratches	34

List of Tables

2.1	Crystalline phases of silicon and respective pressure region. Adapted from [21].	7
4.1	Experimental plan defined for all scratch experiments	20
5.1	Residual scratch depths for each indenter set	22
5.2	Raman intensity ratio and depth of cut	27

List of Abbreviations

a-Si	amorphous silicon
CMOS	Complementary Metal Oxide Semiconductor
c-Si	crystalline silicon
DWS	diamond wire sawing
dtb	ductile-to-brittle
HSK	Hollow Shank Taper
IWF	Institut für Werkzeugmaschinen und Fertigung
LAS	Loose abrasive slurry sawing
MWS	multi-wire sawing
PV	photovoltaic
SEMI	Semiconductor Equipment and Materials International

List of Symbols

Symbol	Unit	Description
b_a	[-]	half-power bandwidth of peak for amorphous phase
b_c	[-]	half-power bandwidth of peak for crystalline phase
d_c	[mm]	critical depth of cut
$f_{Ga(\nu)}$	[-]	Gaussian fit for amorphous peaks
$f_{Lc(\nu)}$	[-]	Lorentz fit for crystalline peaks
h_a	[-]	height of peak for amorphous phase
h_c	[-]	height of peak for crystalline phase
I_a	[-]	Raman intensity of amorphous silicon
I_c	[-]	Raman intensity of crystalline silicon
n	$[\frac{1}{min}]$	spindle speed
r	[-]	Raman intensity ratio
r_i	[mm]	inner radius
r_o	[mm]	outer radius
v_c	$[\frac{m}{s}]$	cutting speed
v_f	$[\frac{mm}{mm}]$	feed speed
ρ	$[\frac{g}{m^3}]$	density
ν	[-]	Raman shift

Introduction

1.1 Motivation

To meet more the demand for sustainably sourced energy, the reduction of using conventional sources of energy and the increasing concern for the environment, researchers are putting their efforts into making solar energy a viable option of renewable energy, with low cost and high efficiency [1]. To produce photovoltaic cells, single crystal silicon is one of the most popular materials used. About 12% of the total cost production of photovoltaic cells comes from the wafers [2] and 80% of the solar cells production is based on silicon bulk crystals [3]. Therefore, the improvement of manufacturing silicon for photovoltaic technology results in cost reduction. Silicon wafers are produced by a multi-wire sawing (MWS) machine. In this process, a silicon ingot is pressed into a wire web, and the abrasives on the moving wires cut the ingot into hundreds or thousands of wafers in a single pass [4]. Diamond wires are used for sawing because they can improve the quality of wafers. The material removal mechanism is the abrasive wear between two bodies, leading to surfaces with distinct morphology [4] and for diamond wire sawing (DWS), since the abrasives are fixed on the wire, they scratch over the crystal surface [5]. Despite its importance, it is still not fully understood how the process parameters affect the surface quality, to obtain a wafer without cracks and no warping [6].

1.2 Related Work

A lot of work has been done to understand the material removal fundamentals in order to optimize the wire saw machining process. Among other things, the tool wear, forces and surface quality have been focused on. It has been demonstrated that the influences of process parameters can be determined by scratch tests, which simulate the interaction between the tool and workpiece with good fidelity to the real process outcome, in particular researches focusing on characterizing material removal via analysis of the surface and sub-surface.

1.3 Overview

The aim of this thesis is to analyze the material removal mode and phase transition, as well as quantifying the residual crystalline structure, when machining mono-crystalline silicon with diamond indenters. First, an overview of the important theoretical aspects is given, then the experimental setup - which has been developed - and the measurements performed are described, as well as the results obtained and discussion for this and further research.

Literature review

This chapter is dedicated to the theoretical background concepts needed in this thesis and a literature review of the most recent scientific work done in this specific research area.

2.1 Monocrystalline silicon and wafers

Silicon (Si), element 14 of the periodic table, is the second most abundant element on earth crust. It crystallizes into a diamond cubic crystal structure, composed of 18 atoms of silicon, as shown in Figure 2.1(a) [7]. In addition to the atomic arrangement, the silicon crystal is also described by its various planes passing through the atomic location defined by the Miller Indices. Thus, the silicon crystal has its crystallographic planes defined in three main groups: (100), (110), and (111), as illustrated by Figure 2.1(b)[8]. In case of a single crystallographic orientation, that is, the crystal lattice is continuous and free of any grain boundaries, the material is defined as a monocrystalline silicon [5].

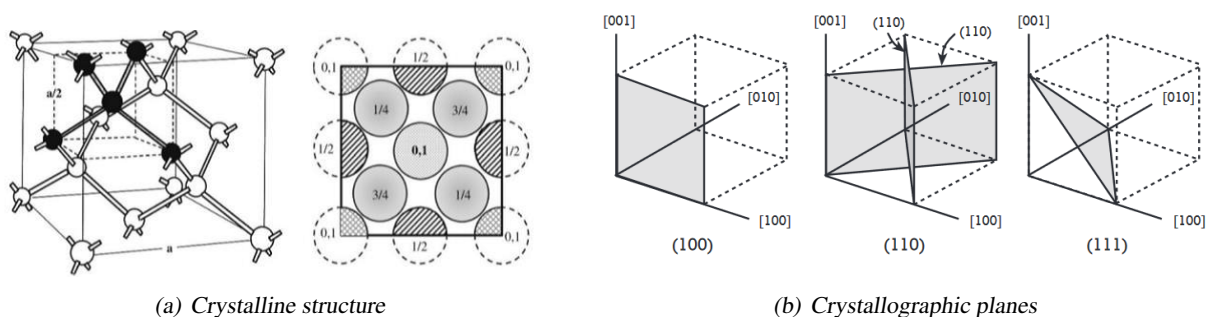


Figure 2.1: (a) Crystalline structure of silicon in the projections tree-dimensional and bi-dimensional [8] and (b) Crystallographic planes of monocrystalline silicon [9]

Silicon is a hard, brittle material - at room temperature - under tensile stress, silicon single crystal (or monocrystalline silicon) fractures suddenly without significant plastic deformation [10]. Its properties

depend on the crystallographic orientation relative to which they were measured, making it an anisotropic material [6]. Silicon is widely used for the fabrication of solar panels wafers and electronic microchips due its semi-conductive behavior [11]. The atomic arrangement of each of the silicon orientations is different from each other. A diamond cubic crystal should be much more easily broken parallel to a (110) surface than parallel to either a (100) and (111) surface [12]. Therefore, the wafers production for specific applications also depends on the crystallographic orientation: (100) and (111) - surface parallel to the unit cell face and intersecting three opposite corners of the unit cell, respectively - are the essentially the only ones used for device fabrication and since substrates with (110) planes are of no real practical used, it is very rare to find components with this orientation [11, 12]. From these orientations, (100) is much more common since it is used exclusively for fabrication of CMOS (Complementary Metal Oxide Semiconductor) devices [12]. Defects on the wafer surface (scratches, mechanical damage, etc.) can cause premature cracking under stress. Hence, silicon wafers having a rough surface or residual damage left (cut wafer, lapped wafer) are more prone to break compared with polished wafers, which are extensively standardized by Semiconductor Equipment and Materials International (SEMI), leading to a surface free of mechanical damage [13].

2.2 Silicon wafers machining

While the ductile or brittle material removal behavior depends on the machining conditions, ductile machining of silicon is possible at small cutting depths [14]. Observing Figure 2.2, one can see that with the workpiece being cut and at the beginning of cut (cutting direction illustrated), hence small depth of cut, the material is behaving ductile and therefore the surface is smooth. As the machining proceeds and the depth is increased, it is possible to see the moment when the first crack occurs - this is called the critical depth of cut (d_c). From this point on the transition to brittle machining occurs, leading to micro-fractures and cracks at the surface [15, 16].

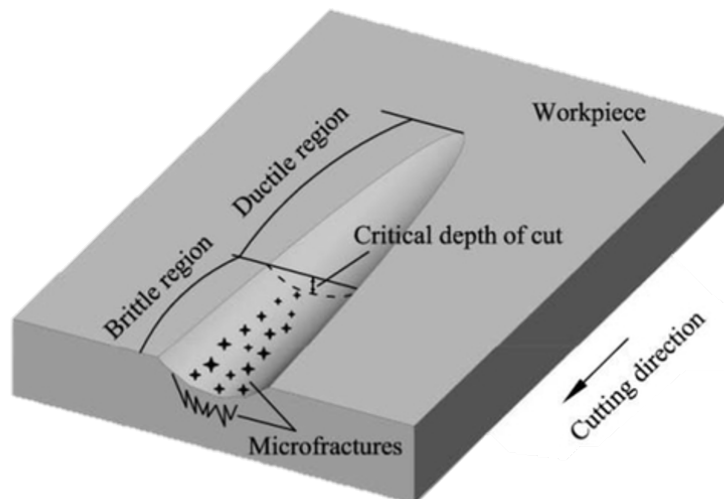


Figure 2.2: Schematic of critical depth of cut identification. Extracted from [16]

Silicon wafers are produced by wire sawing. In this process, a silicon ingot is pressed against a wire web, and the abrasives on the moving wires cut the ingot into hundreds or thousands of wafers in a single pass, simultaneously [17]. There are two main wire sawing techniques: slurry and fixed abrasive wire (diamond wire sawing DWS).

2.2.1 Loose abrasive and diamond wire sawing

In loose abrasive slurry sawing (LAS), the cutting is done by feeding a slurry containing abrasive, silicon carbide particles on the wire web. The ingots are pushed against the wire web - either up or downward - until the cut is finished [5]. Silicon material is continuously removed there through the interaction of the SiC particles with the silicon surface. In the loose abrasive sawing, the wires move in one direction with a speed between 10 and 20 m/s and cutting speed up to 0.5 mm/min, which yields a total cutting time of about 8–13 h for a standard ingot size (56 mm × 56 mm) [4].

Recently, diamond-abrasive coated wires have been used for the fixed abrasive sawing technique: where the abrasives are fixed on the wires and the slurry can be replaced by a water based coolant [4, 10]. Fixed abrasive sawing uses a steel wire coated with diamonds - DWS, which are the responsible for achieving the cut. This technique allows much higher cutting speeds and requires less wire and only a cheap cooling fluid such as water. It is an improvement of the sawing technology that has been used in production of 90% of photovoltaic (PV) wafers [4]. The wires can remove more volume but the diamond-coated wires are more expensive but the cutting time for silicon can be reduced to 2-3h. There is general agreement that the fundamental process is the removal of material by scratching the particles on the wire over the crystal surface [5]. The two different process (LAS and DWS) can be seen in Figure 2.3

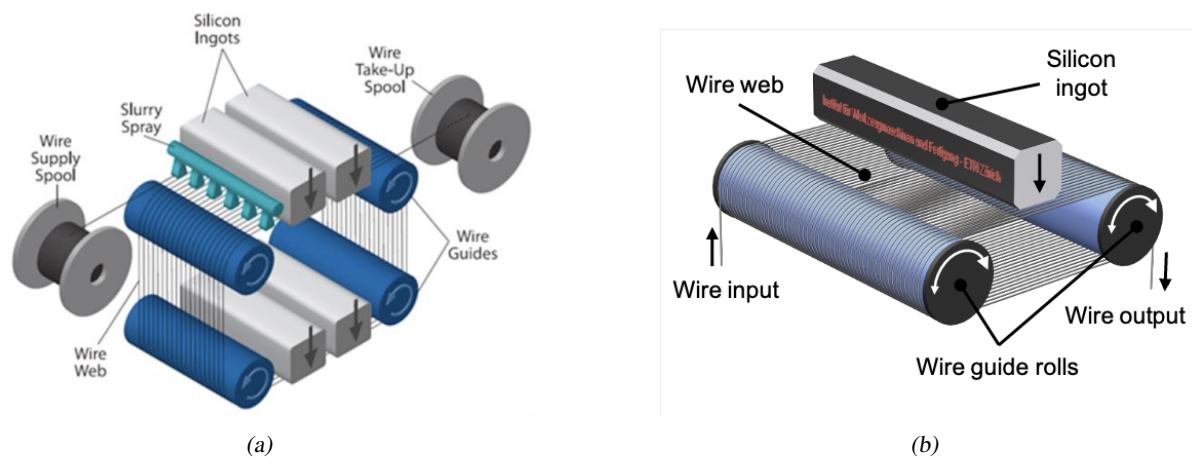


Figure 2.3: (a) Loose abrasive slurry sawing (extracted from [1]) and (b) diamond wire sawing

Thus, different sawing techniques lead to different material removal mechanisms. LAS is rolling-indenting grains and therefore fracture induced removal (more brittle fractures), whereas DWS is a scratching grain (see Figure 2.4), leading to a mix of ductile and brittle removal, depending on penetration depth [5]. The pressure present leads to phase transitions which is believed to enable ductile removal.

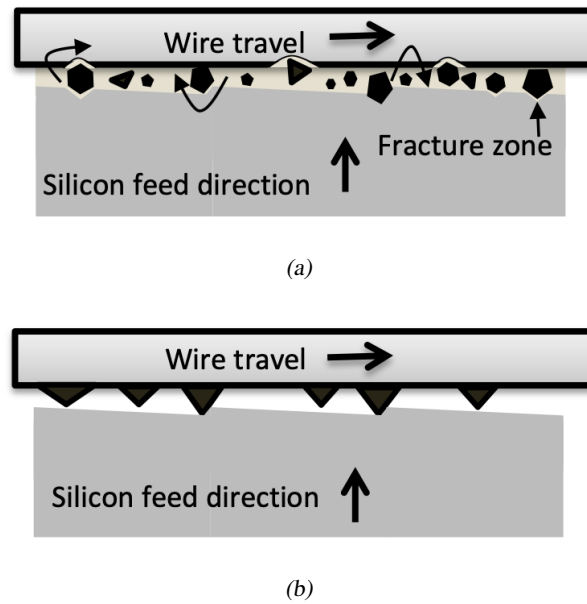


Figure 2.4: Material removal mechanisms in (a) Loose abrasive (extracted from [1]) and (b) diamond wire sawing of silicon

2.2.2 Phase transitions

In silicon, ductile-regime machining (movement of dislocations and plastic deformation of the crystal) comes along and is possible due to pressure-induced metallization under the cutting tool [18]. Silicon phase transformation can be induced during the process due to the extremely high hydrostatic stress that can be produced, exceeding the new phase transformation pressure. At atmospheric pressure, silicon has a cubic diamond structure (labeled Si-I). At room temperature, this structure persists up to ~ 11 GPa, and at atmospheric pressure, from 0 K to its melting point of 1683 K [19]. Under higher pressures though, 11 other crystalline phases of Si have been identified [20]. Most of these phases can exist only at very high pressures and are, therefore, outside the scope of this discussion and some are thermodynamically stable when pressure exceeds some critical values and form directly from the cubic phase [21]. Of interest of this work are the phases referred S-II (β -tin structure), Si-III (body-centered cubic structure, with 8 atoms per unit cell), Si-IV (hexagonal diamond structure), Si-IX (tetragonal structure with 12 atoms per unit cell) and Si-XII (rhombohedral structure with 8 atoms per unit cell) [20].

Figure 2.5 shows a schematic of the phase transformations occurring in silicon under static contact loading and during subsequent annealing. Si-I is the only thermodynamically stable phase at ambient conditions. Fast unloading rates (> 1 mm/min) imply no sufficient time for the reconstruction of the Si lattice during pressure release, leading to lattice disordering which leads to the formation of amorphous material, instead of the kinetically controlled Si-II \rightarrow Si-XII phase transformation [20]. The conditions and respectively structures for each one of the 12 phases of silicon is described in Table 2.1

In the pressure range of 9 to 16 GPa, the irreversible transition of Si-I to Si-II occurs [19, 22]. The irreversible plastic deformation in monocrystal silicon only occurs with the initiation of this metallic phase. Upon unloading a metallic tetragonal-body-centred to amorphous phase transformation is observed and supported by studies using electrical resistance, x-ray diffraction, Raman spectroscopy and optical properties [22]. From Si-II the transition to other phases as Si-III, Si-IV, Si-IX and Si-XII upon pressure release is identified. The first phase to form at 10 to 12 GPa is Si-XII and on further

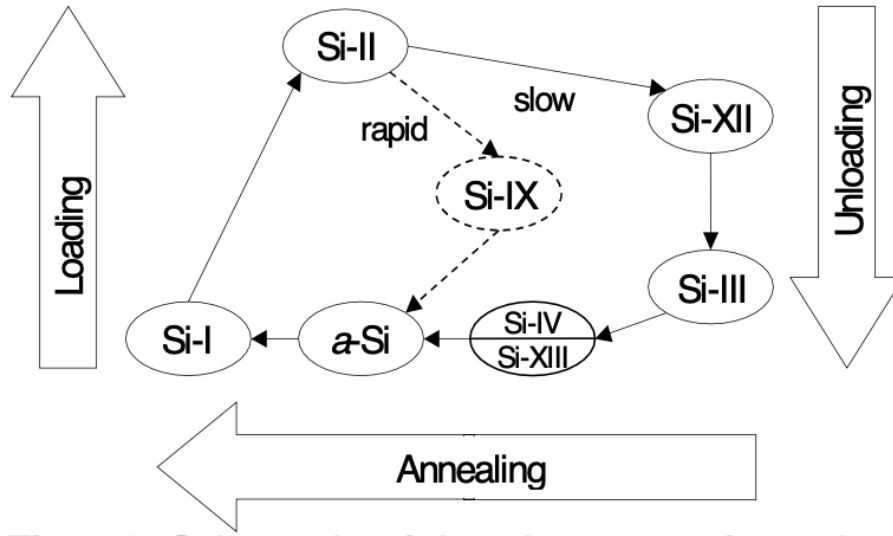


Figure 2.5: Schematic of the phase transformations cycle in silicon under contact loading [20]

Notation	Structure	Pressure region (GPa)
Si-I	Diamond cubic	0-12.5
Si-II	Body-centered tetragonal (<i>beta</i> -Si _{II})	8.8-16.0
Si-III	Body-centered tetragonal (basis of eight atoms)	2.1-0
Si-IV	Diamond hexagonal	-
Si-IX	Tetragonal (12 atoms per unit cell)	12-0.0
Si-XII	Trigonal (8 atoms per unit cell)	12-2.0

Table 2.1: Crystalline phases of silicon and respective pressure region. Adapted from [21].

pressure release the degree of rhomboedral distortion reduces gradually, producing a mixture of Si-XII and Si-III (pressure release from 10 to 0 GPa) [20, 23]. This transformation is fully reversible by recompression to 2.5 GPa [20]. When it comes to Si-IV transformation, this phase can be obtained either from the metastable phase after heat treatment or from Si-I after plastic deformation [20]. The first direct structural observation of hexagonal Si (Si-IV) was made in 1986 a HREM study of the plastic zone around Vickers indentations made in silicon at a temperature of 450 °C [19]. According to Pirouz et al., [19] this cubic-to-hexagonal phase transformation is martensitic: although the hexagonal diamond structure in silicon is not a thermodynamically stable phase, its diffusionless mechanism and crystallographic characteristics - such as the interface between the transformed and the untransformed regions remain approximately planar (a salient feature of martensitic transformation) - make the transformation a martensitic one [19, 24, 23]. Cannon [25], using X-ray diffraction with synchrotron sources, has shown that the transformation sequence with the increase of the pressure is

$$I \rightarrow II \rightarrow XI \rightarrow V \rightarrow VI \rightarrow VII \rightarrow X.$$

Due to the density difference within the phases, a volume change occurs during phase transition. It was

found that $\rho_{\text{Si-XII}} > \rho_{\text{Si-III}} > \rho_{\text{Si-I}} \sim \rho_{\text{Si-IV}} > \rho_{\text{a-Si}}$ [18]. The Si-I \rightarrow Si-II transformation is followed by $\sim 20\%$ densification of the material. Upon slow decompression, Si-II \rightarrow Si-XII leads to $\sim 9\%$ volume expansion, with $\sim 2\%$ recovered from the Si-XII \rightarrow Si-III gradual transformation at low pressures, due to the equilibrium Si-III structure was found to be $\sim 9\%$ denser than Si-I and $\sim 2\%$ less dense than Si-XII. Finally, the hexagonal diamond Si-IV phase has an atomic volume identical to that of Si-I. Due to this density difference and residual stress, silicon wafers can bend during or after machining when the conditions changes during the process or between the two faces, see Figure 2.6 which leads to more post-processing or wafer to be unusable.

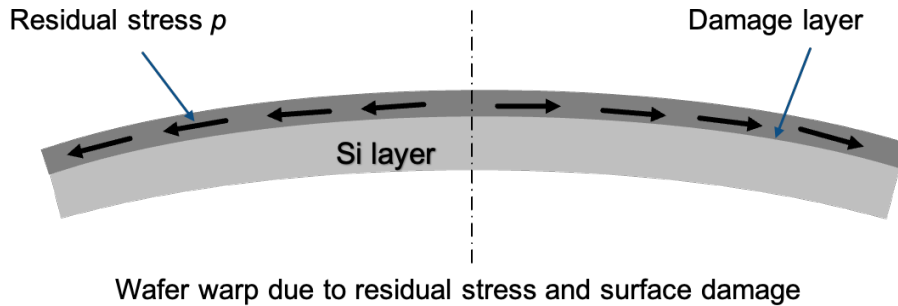


Figure 2.6: Wafer warp due to residual stress and surface damage [26]

2.2.3 Raman spectroscopy

Raman spectroscopy has been established among optical methods as a fast, sensitive and nondestructive method for the investigation of the crystallinity. It provides structural information, like the identification of materials and composition since the Raman frequency is characteristic for material, structure and mechanical forces, which have an effect on the sample [27]. The term "Raman scattering" refers to inelastic scattering by most elementary excitations associated with the degrees of freedom of electrons in crystalline and amorphous solids [28].

Every Raman spectrum has a very intense band at 0 cm^{-1} caused by Rayleigh line (elastically scattered light), which is normally suppressed by using appropriate filters. At positive wavenumbers, stokes bands are observed whereas the anti-stokes bands are observed in negative wavenumbers. Crystalline materials can undergo lattice vibrations and the corresponding Raman bands are strongly dependent on the local symmetry: this is the explanation why amorphous materials bands are broader than those of crystalline materials [27]. The intensity is related to the difference in frequency between the scattered light and the incident electromagnetic radiation [29]. It is important to choose the light source correctly because different wavelengths have different penetration depths into the sample surface, which allows the information acquisition from different depths by using a different laser. For example, for light emitted with a wavelength of 532 nm and a silicon sample, a penetration depth of 935 nm is achieved.

The typical information collected from the Raman is presented in Figure 2.7. The full width at half maximum (FWHM) gives information about the crystallinity of the peak, considering that broad peaks indicate amorphous phase whereas sharp peaks are characteristic from crystalline phases. Stress and deformation information can be extracted from the band position shift and a lot of work has been conducted in this area. The intensity defined as the integration area under the peak gives information about the concentration of the given phase.

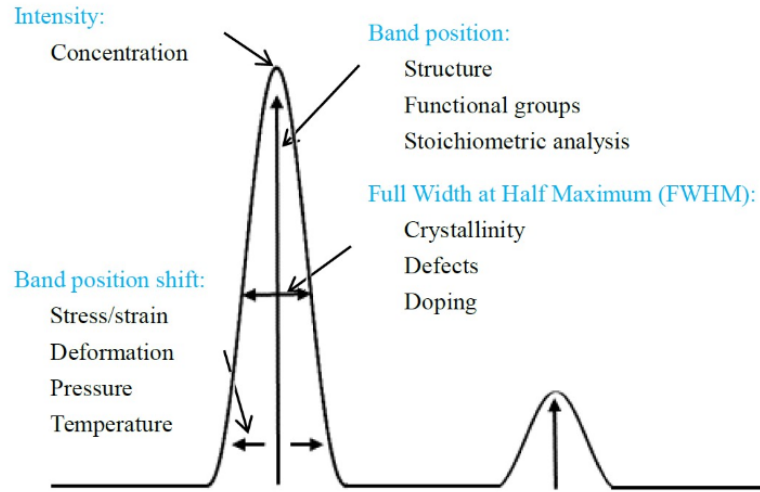


Figure 2.7: Typical information of Raman spectra and corresponding material information [30]

For silicon, in the absence of stress, the first-order Raman spectrum of Si-I exhibits a single line at 520 cm^{-1} . For amorphous silicon, an optical band peak at 470 cm^{-1} is displayed in the first order Raman spectra, see Figure 2.8.

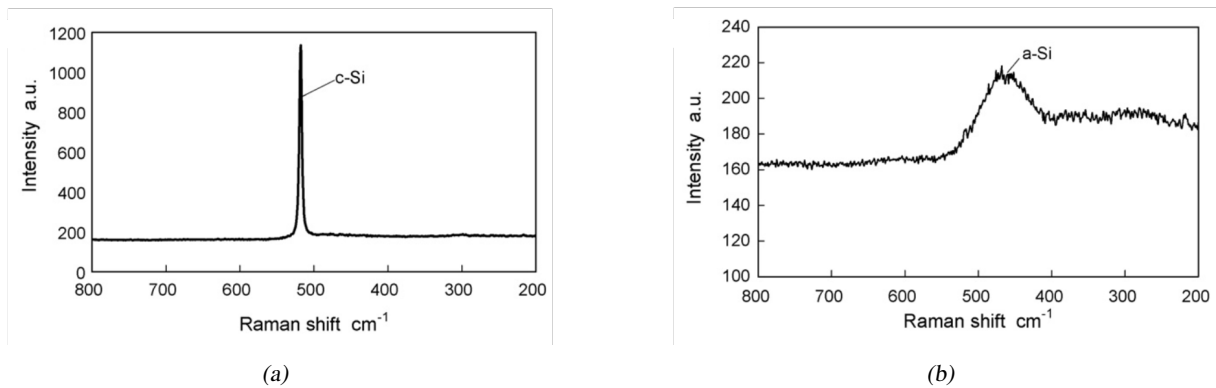


Figure 2.8: Raman spectra showing (a) only crystalline peak and (b) amorphous peak [31]

Intensity ratio

Yan proposed a new parameter for the quantification of crystalline phases by means of Raman spectroscopy, namely the Raman intensity ratio r [31]. The parameter is defined by

$$r = \frac{I_a}{I_c} \quad (2.1)$$

where I_a is the total Raman intensity of the amorphous silicon and I_c is the total Raman intensity of the crystalline silicon. It can be seen that the bigger the value of r , the thicker the amorphous layer. By definition, I_a and I_c are the integrals of amorphous and crystalline peaks. The proposition of the parameter first takes in consideration the overlapping of peaks and separate them by using the curve fitting technique. Due to the shape of each peak, the Gaussian distribution is suitable for fitting broadband

curves as the amorphous one whereas Lorentzian distribution is suitable for describing the line shape of spectral lines, as the crystalline peaks. Lorentz and Gaussian distribution along with the amorphous intensity ratio equations are given in Equations (2.2) to (2.4), respectively, extracted from [31]. In all cases, ν is the Raman shift h is the height and b is the half-power bandwidth, with "a" and "c" indicating whether these parameters are from amorphous or crystalline phases and can be simply readout from the individual Gaussian and Lorentz curves. An example of curve fitting and how this assumptions works with a real silicon spectrum can be seen in Figure 2.9.

$$f_{Lc}(\nu) = \frac{h_c}{1 + (\nu - \nu_c)^2/b_c^2} \quad (2.2)$$

$$f_{Ga}(\nu) = h_a \exp\left(-\frac{(\nu - \nu_a)^2}{b_a^2}\right) \quad (2.3)$$

$$r = \frac{\int f_{Ga}(\nu) d\nu}{\int f_{Lc}(\nu) d\nu} = \frac{h_a b_a \sqrt{\pi}}{h_c b_c \pi} = \frac{1}{\sqrt{\pi}} \frac{h_a b_a}{h_c b_c} \quad (2.4)$$

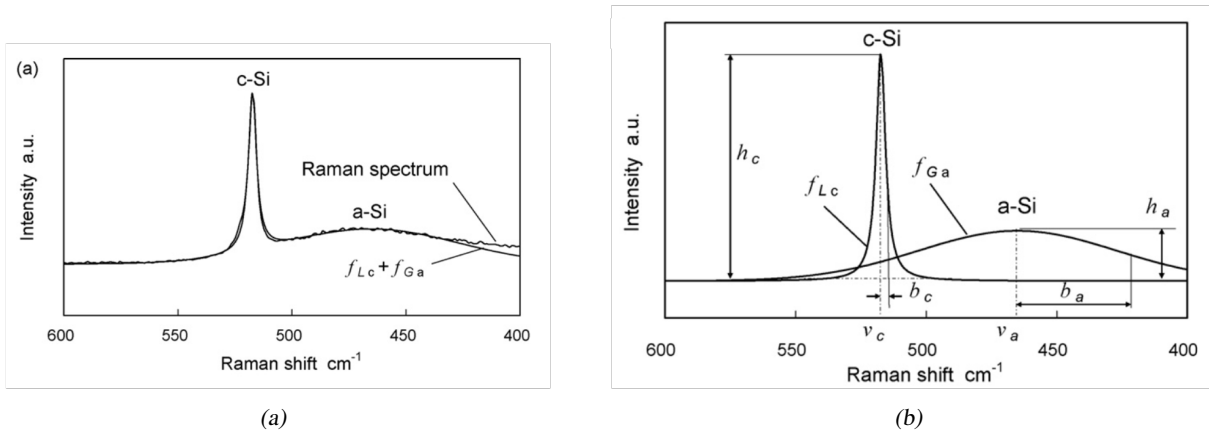


Figure 2.9: Curve fitting method for separating Raman peaks (a) comparison of experimental Raman spectra and fitted curve; (b) separated Raman peaks of amorphous and crystalline silicon [31]

This parameter will be used to quantify the relative significance between two phases in order to give an estimation for the amount of each phase present.

2.2.4 Scratching tests

Recent experimental scratching tests with a single diamond tip on a monocrystalline silicon surface have been developed to study the material removal mechanism, specially for the fixed abrasive sawing process. Because of the size distribution of the diamond particles on the wire (see Figure 2.10), the forces and indentation depth varies and thus the material that is removed also vary during the process. Hence, the importance of knowing the influence of these parameters on the process and surface quality [5]. Under normal sawing conditions, the size distribution will also change because particles change the shape and break or are pulled out and this changes the total forces: when the force increases, the number of scratches particles also increases

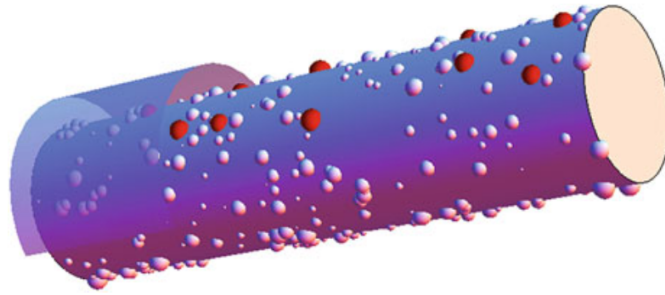


Figure 2.10: Simulation of the number of particles on wire in contact with the crystal surface due to size distribution [5]

There is considerable interest focused on the machining of silicon and process parameters prediction. Gogotsi et al., [32] affirmed in his work that predict the experimental conditions for ductile regime machining of brittle materials from scratch tests is possible, specially for diamond wire sawing. To improve the surface quality, it is important to control the material removal and consequently phase transition. A lot of work has been done concerning scratch tests, specially associated with phase transitions of silicon and low speed scratching experiments is the main responsible for the existing knowledge about the effects of the scratching parameters, indenters shape and crystallographic orientation in phase transformation, material removal and properties.

Gogotsi [33] demonstrated that phase transformations occur in a variety of silicon machining operations, including slicing, dicing and gridding. In another study, he investigate the influence of the type of indenter (Vickers, conical and spherical Rockwell) at a constant scratching speed of $10 \mu\text{m/s}$ and found that material removal depends on the indenter shape. The results shows that by using a sharp tool (Vickers and conical) the material removal mechanism involves ductile removal of the metallic phase to a critical depth of cut while no material is removed during scratching using a blunt tool, with a spherical tip, see Figure 2.11. Additionally, his research reveals that more amorphous silicon is produced at small depths of cut. [32]

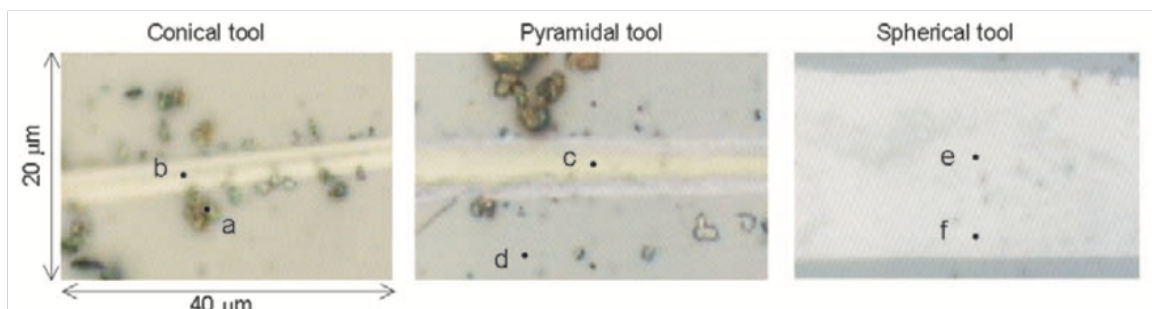


Figure 2.11: Optical micrographs of scratches with different material removal from different tools. Extracted from [32].

The effect of scratching speed on phase transformation in high-speed scratching of monocrystalline silicon was studied by Wang et al., [34]. They reported that with variable loading/unloading rates different phases of silicon were formed. The study also shows that with cutting speed up to 1 mm/min , the unloading rate is not high enough to produce amorphous silicon but only Si-III and Si-XII – those phases were not produced on cutting speeds higher than 1 mm/min . Figure 2.12 shows the Raman spectra of different positions within the scratched grooves made at different scratching speeds.

Furthermore, a larger amount of a-Si was produced at higher scratching speeds and leads to a larger volume expansion of the deformed material. Effects of temperature on the phase transformations of monocrystalline silicon are expected to be insignificant.

Gassilloud [35] studied scratches made at $2\ \mu\text{m/s}$ and $100\ \mu\text{m/s}$, with linearly increasing load – unlike the aforementioned studies, which were performed with constant scratching speed. They found that high scratching speed resulted in the formation of only a-Si, whereas low speed induced also Si-III and Si-XII. which is consistent with the results of Wang [34] of high speed (1 mm/min to 10 000 mm/min) which showed different Si phases produced with variable loading/unloading rates, leading to only a-Si and Si-IV detected at higher speeds.

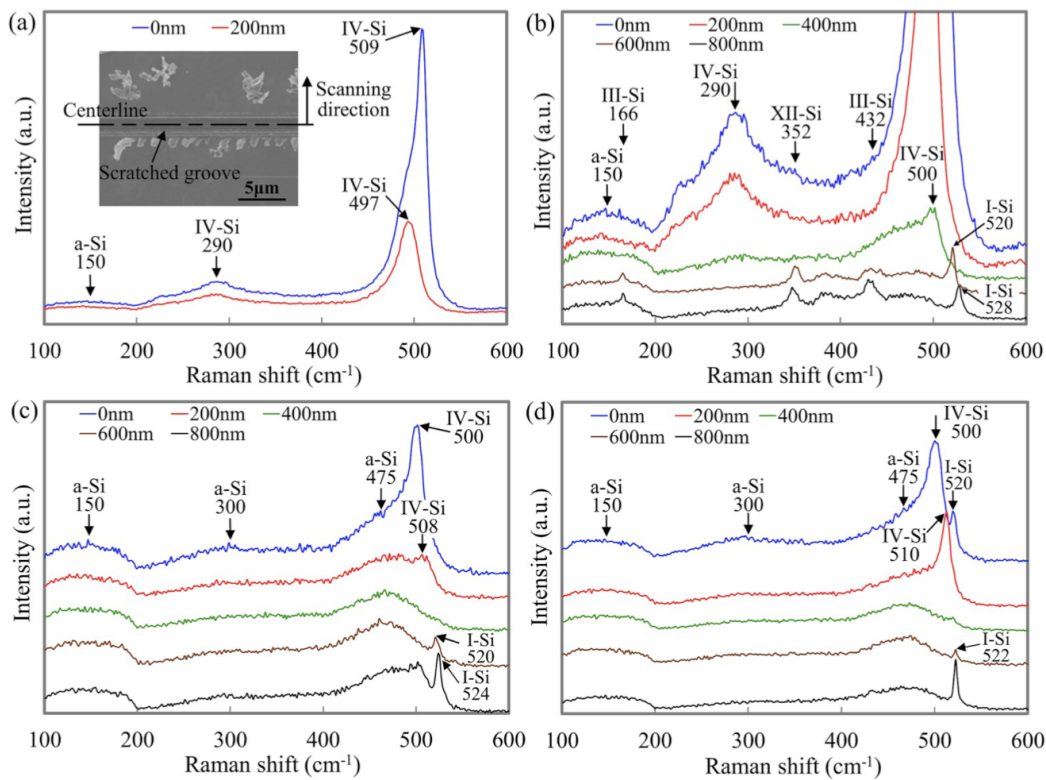


Figure 2.12: Raman spectra of different positions within the scratched grooves made at (a) 1 mm/min, (b) 1 mm/min with a smaller scale of Raman spectra intensity than Fig. a, (c) 10 m/s and (d) 20 m/s (the 0–800 nm in all legends indicates the distance from the scratch centerline). Extracted from [34]

A study about the effects of indenter orientation, load, and scratching speed on deformation peculiarities under nanoscratching of Si was performed by Shikimaka et al. [36]. They reported lower values of scratch hardness - resistance to a sharp object as it moves against the surface - and more intensive brittle fracture on edge-on scratching in comparison to face-on scratching (see Figure 2.13), which is presumably caused by easier displacement of material directly sideways along two faces.

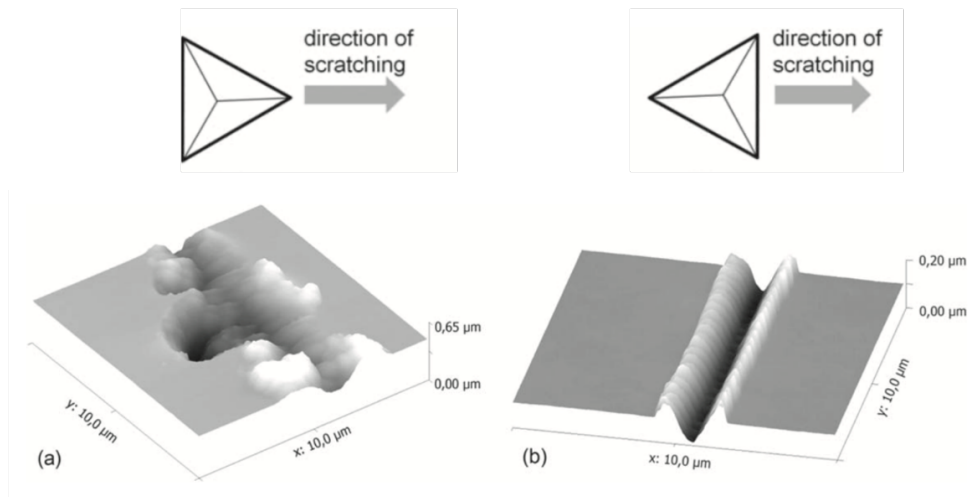


Figure 2.13: 3D AFM images of scratches (a) edge-on orientation of scratching (E-scratching) and (b) face-on orientation of scratching (F-scratching). Extracted from [36]

Research gap

The state of the art identifies effects of scratching speed and indenter shape on phase transition and material removal mode. The vast majority of research done so far perform scratches in a small range of speed, which does not adequately describe the sawing process that uses cutting speeds up to 35 m/s - significantly higher and there is not much detailed study of the effects at high speed.

Thus, there is still a gap in the fundamental understanding of silicon behavior under high scratching speeds and if this potential effect corroborates with the different indenter shape due to the lack of combination of experiments of this with high scratching speed. Therefore, the question is whether the indenter shape has a significant effect on the residual phase at high speed.

Also, it is important to summarize that material removal mode and residual phase are important conditions to focus on, since ductile mode promotes better surface quality but is associated with phase transition and different phases of silicon have different densities, leading to residual stress and possible warping of the wafer.

Materials and methods

This chapter is dedicated to the materials and methods used. The experimental setup developed at the Institut für Werkzeugmaschinen und Fertigung (IWF), the definitive experimental plan and procedure are described.

4.1 Silicon workpiece

Although multicrystalline silicon is cheaper and expected to lower the costs in the PV-industry, its cells are much less efficient and its machining is confronted with many challenges (grain boundaries and more crystallographic defects) [17]. As a consequence, the vast majority of all cells are c-Si and is the interesting case and all the experiments were carried out with the same monocrystalline workpiece with 100 mm diameter, attached to a Hollow Shank Taper (HSK) tool holder (see Figure 4.1) at the institute. To obtain a clear analysis of the ductile to brittle transition in the scratches, the surface of the workpiece was polished externally in several steps, in order to obtain a mirror-like surface. Because of this process, a slight parallelity error and a shape deviation were induced into the surface. In order to find the exact local contact point with the surface, which changes due to these errors when moving in radial direction, a single touching scratch was performed prior to each scratch series.

Although the crystallographic orientation is also relevant for the ductile-to-brittle transition, it wasn't measured in the experiments due to the perpetual rotation of the workpiece with the spindle, which made the orientation to change continuously and therefore impeded an exact determination.

4.2 Cutting tool and experimental setup

The scratching experiments were conducted using eleven different scratching tools in three standardized hardness testing geometries. The tools used has three different shapes: Vickers, Berkovich and Rockwell, provided by the Eugen Buob company, see Figure 4.2

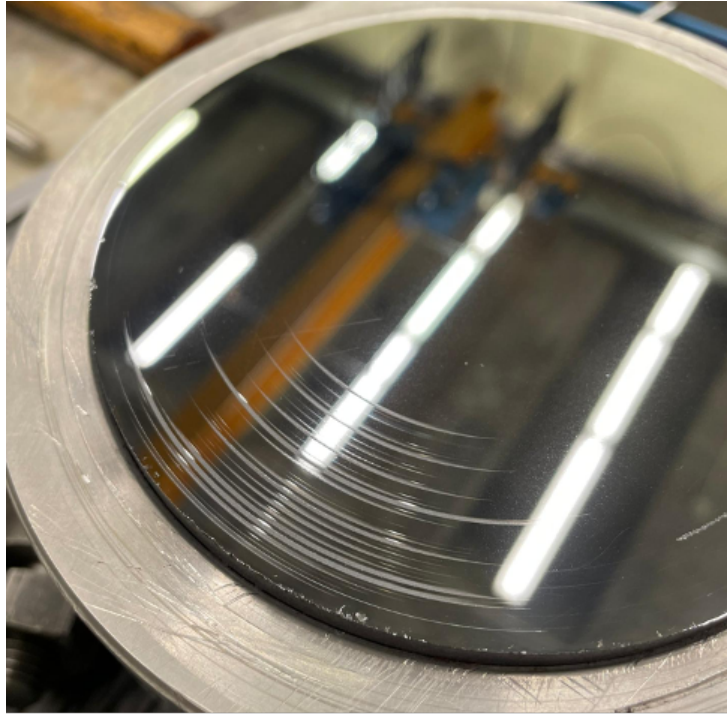


Figure 4.1: Silicon workpiece used for the experiments; the scratches can be seen on the surface as thin white lines

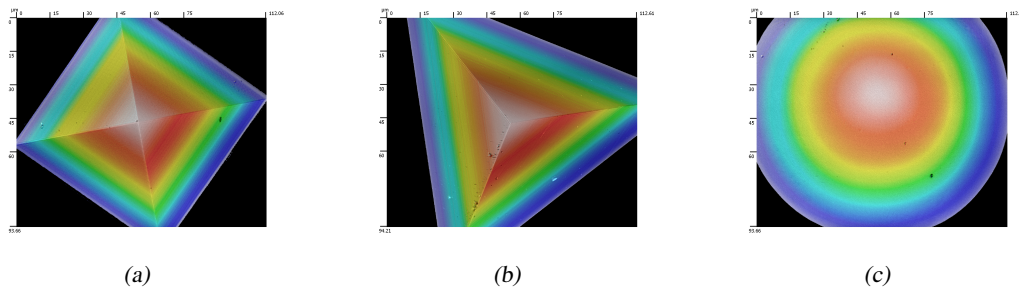


Figure 4.2: Sensofar Microscope images of (a) Vickers (b) Berkovich and (c) Rockwell indenters with 150x magnification

The indenter was fixed on a force measurement platform, on the table of a Fehlmann Picomax Versa 825 five-axis milling machine (see Figure 4.3). This machine was chosen due to its comparably high stiffness and precision, allowing to clamp the heavy workpiece and rotate it stably at high speeds. During the experiments, the spindle with the Si workpiece was moved down and sideways, producing approximately 10 scratches per run, as is shown in Figure 9. The resulting kinematics is that of a face-turning process with no overlapping tool traces - therefore the resulting scratches would have the shape of a spiral if they were not interrupted, with scratch length varying from 10 to 30 μm , from the first to the last scratch in the serie. The cutting speed was fixed at $v_c = 25 \text{ m/s}$.

The orientation of the indenter was also changed. Experiments were conducted with 0° (edge-on type of scratches) and the other part conducted with 45° and 180° for Vickers and Berkovich, respectively (Figure 4.4). This positioning changes the direction from where the material was coming, relative to the direction of scratching.

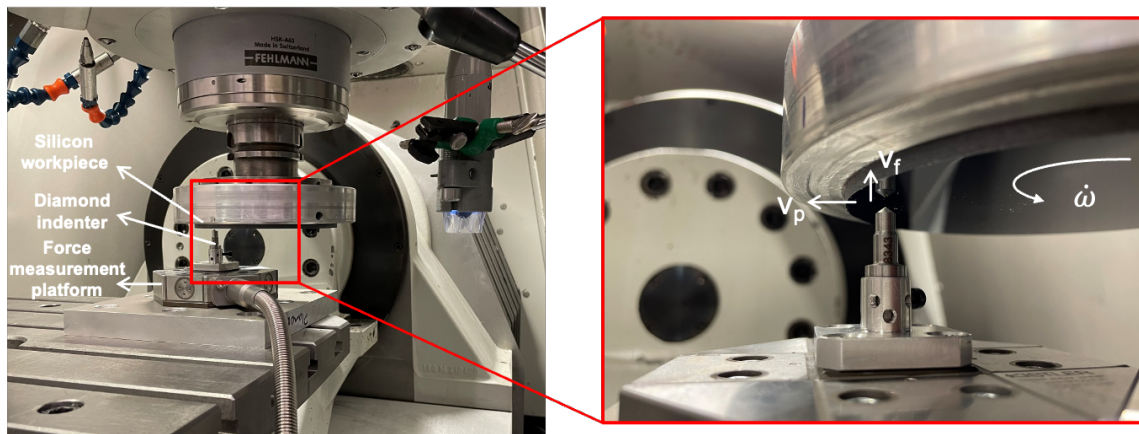


Figure 4.3: Experiments setup: diamond indenter attached fixed to the force measurement platform under the silicon workpiece attached to the spindle

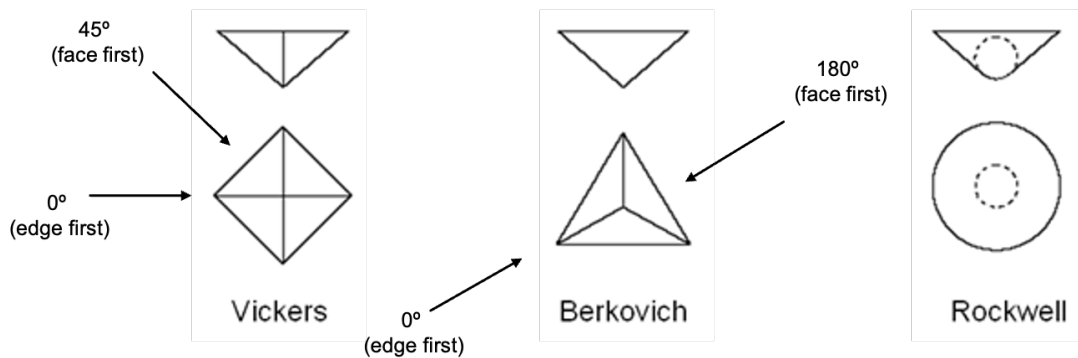


Figure 4.4: The scheme of the Berkovich and Vickers orientation relative to the direction of scratching. Adapted from [20]

4.3 Measurement instruments

The forces were captured with a three-component piezoelectric force dynamometer (Kistler Type 9109AA) - a force measurement platform. The analog charge signal from the platform was processed to a charge amplifier (Kistler Type 5090A), where it was low-pass filtered with 1000 Hz before being digitalized with the help of a measurement card (Kistler Type 120000 Hz) running Kistler's *Dynoware* software which then forwards the information to the computer.

The indenters before and after scratching were measured and analysed with the Sensofar Neox S microscope, as well as the scratches overviews and residual penetration depth.

For detecting the residual phases in the scratches, a Raman microscope was used, with a laser of wavelength 532 nm, penetration depth and spot size of 935 nm and 800 nm, respectively. The integration time used was 10 s with 5 accumulations per measurement. The Raman data was exported using ProjectFour software, from WiTec. In the final step of evaluation, a MATLAB code was developed to join the scratch profiles with the spectral data, as well as for post-processing and analysing the spectral data, which includes upload the data of wavelength position and intensity, correcting the baseline and curve fitting.

4.4 Experimental plan

To minimize external influences during the experiments, a experimental plan was developed. Table 4.1 show the definitive experimental executed, where r_i and r_o are the inner and outer radius, respectively, the positions of the scratches series on the workpiece - at which position, in terms of radius of the workpiece, the series started and ended. The parameter n is the spindle speed.

Exp ID	Indenter ID	Indenter Type	Indenter Orientation	v_c [m/s]	r_i [mm]	r_o [mm]	n [min ⁻¹]	v_f [mm/min]
305	8352	Berkovich	0°	25	52.5	53	4547	227.35
306	8349	Berkovich	180°	25	51.5	52	4636	231.8
307	8347	Vickers	0°	25	50.5	51	4727	236.35
308	8347	Vickers	0°	25	49.5	50	4823	241.15
309	8351	Berkovich	0°	25	48.5	49	4922	246.1
310	8348	Berkovich	180°	25	47.5	48	5026	251.3
311	8345	Vickers	45°	25	46.5	47	5134	256.7
312	8344	Rockwell	0°	25	45.5	46	5247	262.35
313	8353	Berkovich	0°	25	44.5	45	5365	268.25
314	8348	Berkovich	180°	25	43.5	44	5488	274.4
315	8346	Vickers	0°	25	42.5	43	5617	280.85
316	8342	Rockwell	0°	25	41.5	42	5753	287.65
317	8351	Berkovich	0°	25	40.5	41	5895	294.75
318	8343	Rockwell	0°	25	39.5	40	6044	302.2
319	8345	Vickers	45	25	38.5	39	6201	310.05
320	8344	Rockwell	0°	25	37.5	38	6366	318.3
321	8349	Berkovich	180	25	36.5	37	6541	327.05
322	8346	Vickers	45	25	35.5	36	6725	336.25
323	8344	Rockwell	0°	25	33	34	7234	723.4
324	8352	Berkovich	0°	25	32	32.5	7460	373

Table 4.1: Experimental plan defined for all scratch experiments

Results and Discussion

This section is dedicated to summarizing the results of the experiments.

5.1 Scratch profiles

The maximum residual scratch depth was determined, where the residual phases were analyzed and will be described in this section.

5.1.1 Residual cutting depth

In the center of the scratch length, where the forces are - in general - higher, the residual depth of scratch was measured for the first 5 scratches of each set of experiments - combination of indenter shape and orientation. The MATLAB code created to process the data, first of all, defines the offset in Z direction and measures the distance to the lowest point of the profile of each scratch - marked in the plot with red star (see Figure 5.1). The microscope overview image of the scratches is plotted together with the profile, for easy identification of scratch and depth. All the scratches overview images and their profiles are found in appendix Chapter A.1

With the overview image and profile of each scratch set, is possible to see the general increase of depth with increasing scratch count (numbering starts from left to right). The counting of scratches was also done with the peak forces signal. For later phase transition evaluation, the focus of residual depth measurement was laid on ductile scratches. From the 20 scratch sets carried out, the depth measurement was performed in 8 (from scratch 2 to 6 of each set), two for each combination of indenter and angle for Vickers and Berkovich. The Rockwell scratches show fracture only, no material removal, consequently the depths were not measured. An overview of the measured residual scratch depth is presented in Table 5.1.

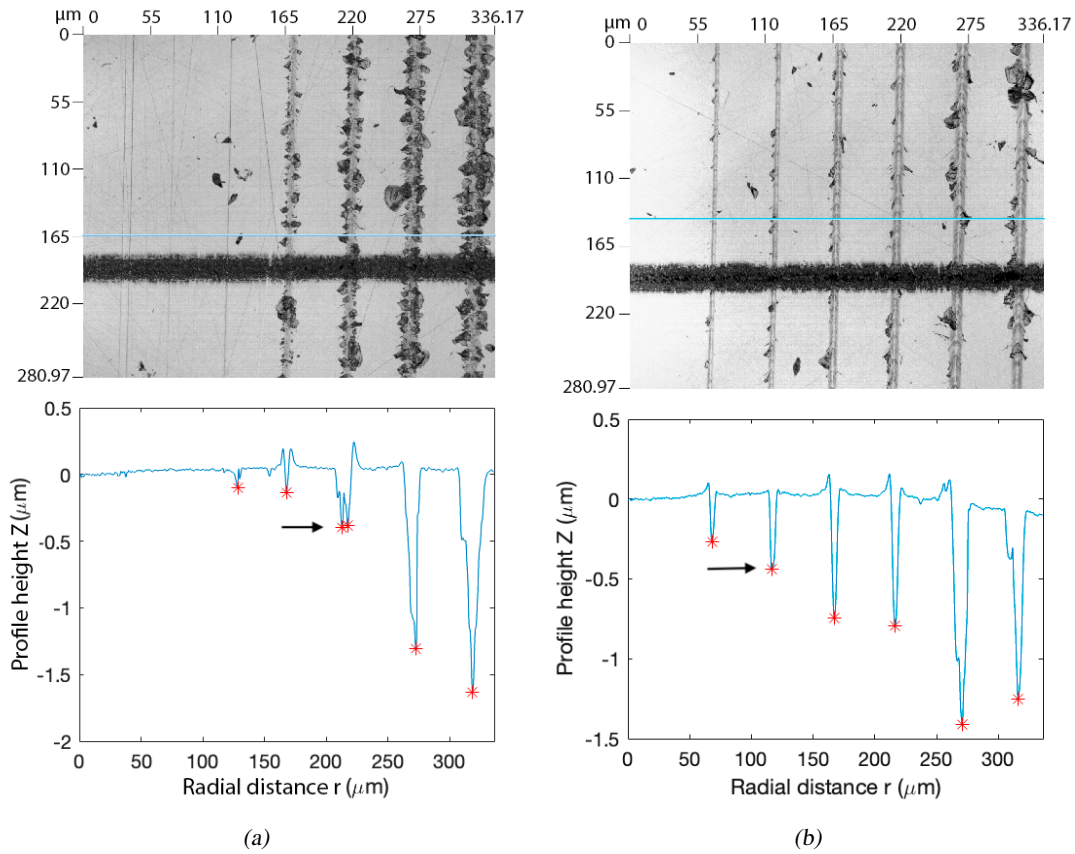


Figure 5.1: Overview and profile of Vickers (a) 0 and (b) 45 degrees

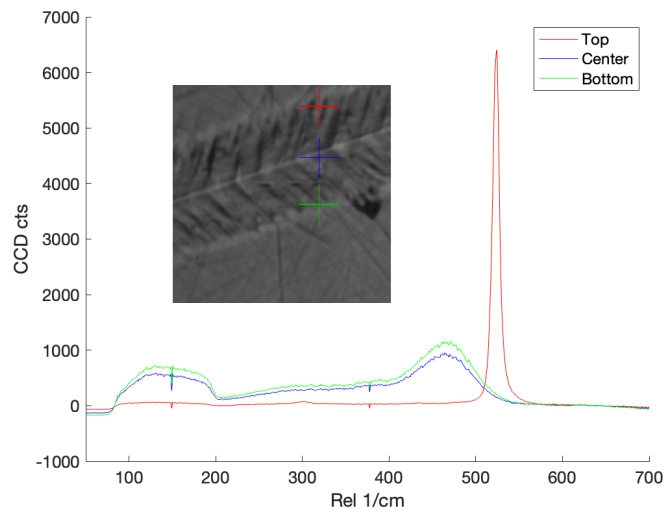
Indenter	Angle	Scratch Series	Residual Scratch Depth Z μm				
			2	3	4	5	6
Vickers	0	308	0.01	0.03	0.31	0.39	0.48
		315	0.03	0.10	0.13	0.40	1.31
	45	319	0.09	0.26	0.47	0.78	0.79
		322	0.44	0.74	0.80	1.41	1.25
Berkovich	0	309	1.80	1.35	2.78	2.94	-
		313	0.006	0.05	0.19	0.80	1.61
	180	310	1.08	0.39	0.18	0.89	2.22
		321	2.04	1.76	1.95	1.91	3.04

Table 5.1: Residual scratch depths for each indenter set

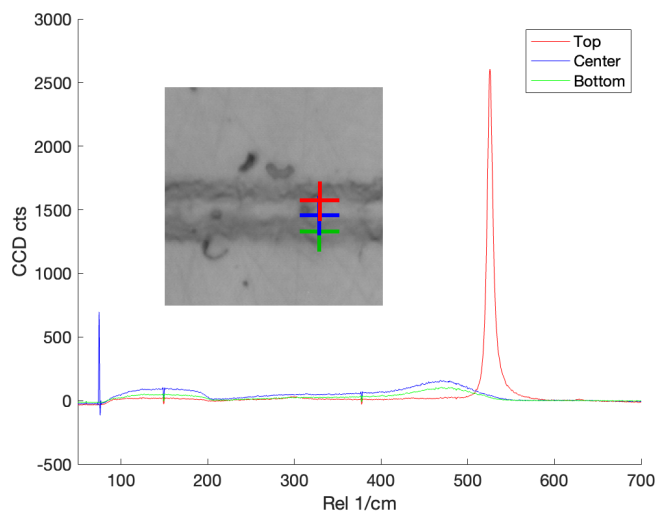
In agreement with Shikimaka [36], the scratches performed with edge-on orientation led to more brittle fracture. Comparing the same depth of cut (approximately $0.4 \mu\text{m}$), marked with the arrow, for both Figure A.2 (a) and (b), it can be seen that more fractures occurred on (a), that represents the Vickers edge-on orientation scratches.

5.1.2 Phase transition and intensity ratio

As mentioned in Section 2.2.2, it is known the extent of phase transformation occurring in silicon at high pressures. Considering the high pressures of scratch tests, Raman microscopy analysis were performed on the scratches to verify the transition that occurs in silicon during ductile mode of cut. Measurements were performed at the top, center and bottom of the groove edge (as it can be seen in Figure 5.2). It was found that the phases at the center of the scratch groove were composed of a-Si and Si-IV. In cases where the spot size of the laser was larger than the scratch width and at test positions near the groove edge, Si-I was also detected. The reason is either that the Raman laser spot overlapped the undisturbed silicon surface - specially for the cases where the measurement were on the top of the groove - or the phase transformation was thinner at this location. Accordingly, the quantitative analysis will only be performed with data from the center of the groove.



(a)



(b)

Figure 5.2: Raman analysis of (a) Berkovich 180° and (b) Vickers 45°

When the groove center is characterized by only a-Si and Si-IV, the amorphization of silicon after the passing of the indenter can be determined by the intensity ratio proposed by Yan et al. [31]. The ratio determines the amount of amorphous silicon present in the area in comparison to the amount of residual Si-IV. For each scratch, 5 measurements in the groove center were performed at the same range of location, in order to evaluate quantitatively with an average of the ratio. For the spectrum and intensity ratio evaluation, a MATLAB code was developed, which corrects the baseline by removing the offset. The data is also filtered with a moving average over datapoints. Finally, the spectrum is decomposed into peaks by a curve fitting. The equation fits a Lorentz curve to the characteristic position of Si-IV peak and a Gaussian distribution to the positions of a-Si. see Figure 5.3(b). The red curve is the fitted curve $f_{Ga} + f_{Lc}$, while the green and pink curve show the separated fits for Gaussian and Lorentz curve, which can be characterized as Raman peaks of amorphous and crystalline silicon. It is important to point out that, by definition, the intensity ratio calculus considers only the amorphous peak around 470 cm^{-1} .

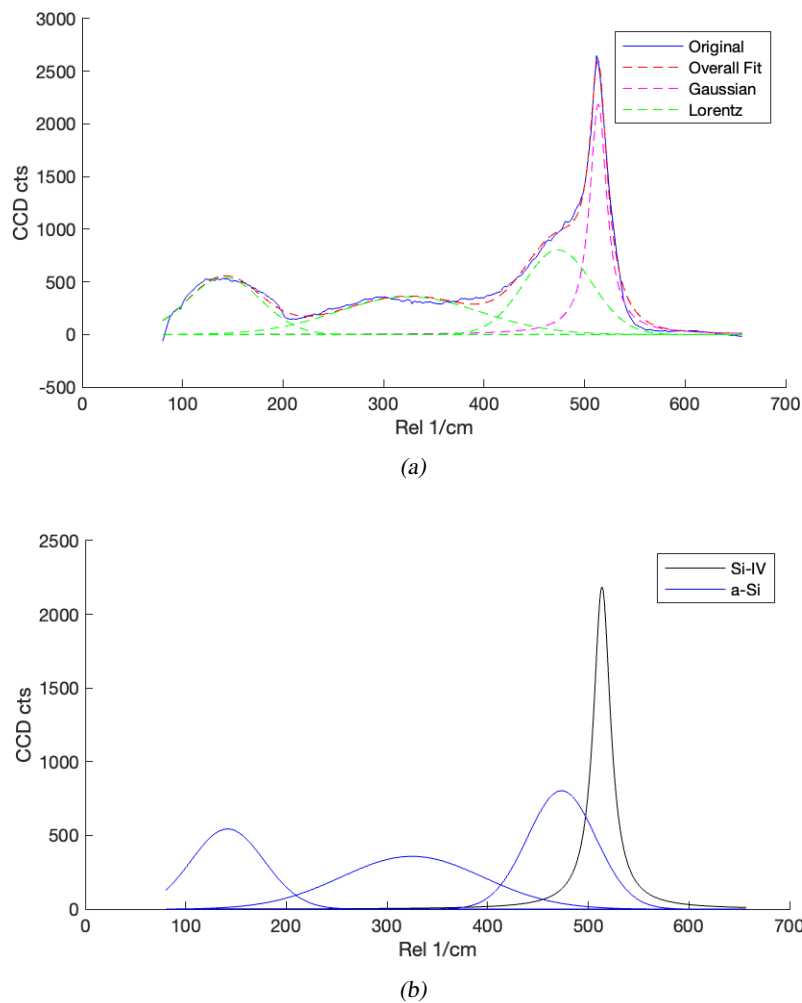
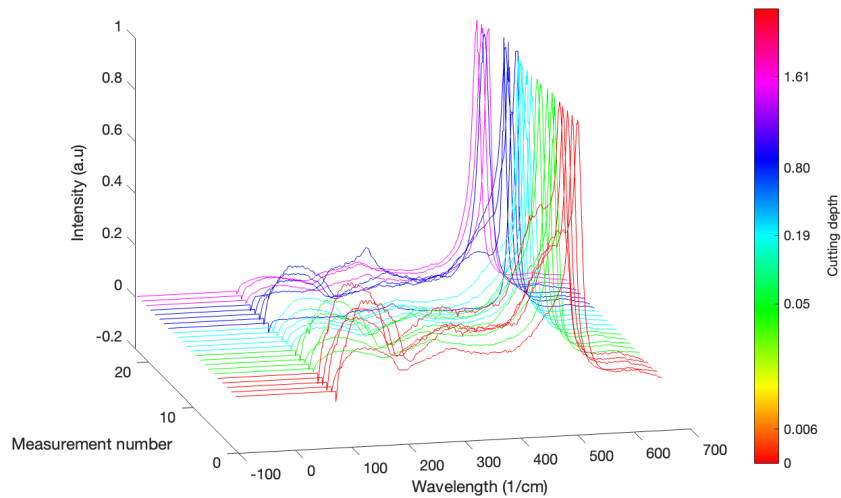


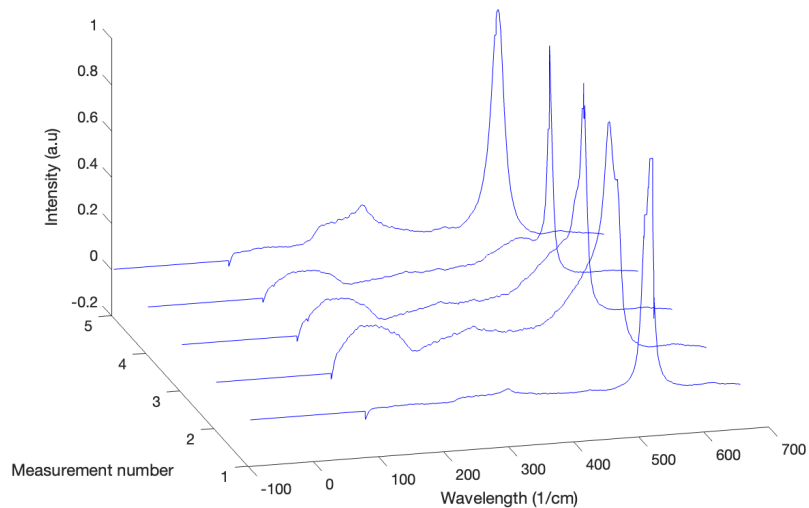
Figure 5.3: Curve fitting method (a) comparison of original experimental Raman data and fitted curve; (b) separated Raman peaks of amorphous and crystalline silicon

For each combination of indenter and orientation angle, the spectra were analysed individually in order to identify and remove possible outliers. To facilitate the analysis of the same scratch series spectra, a 3D plot has been constructed, in which all repetitions are plotted and the depth of cut increases along the y-axis. Each color represents a scratch depth - repetitions of measurements in the same position of a

single scratch. In this case, the intensity axis (z-axis) was normalized to the highest peak. It can be seen from Figure 5.4(a) that for scratches performed with Berkovich 0° indenter, the measurements plotted in blue (specially the last one) exhibits a different peak distribution, with a sharpest peak around 300 cm^{-1} that can be characterized as a si-III peak and it does not have the amorphous peak around 470 cm^{-1} (Figure 5.4(b)), which makes the calculation of the ratio not possible, since this condition is not met. Outliers, therefore, are those measurements where it is not possible to identify a clear Si-IV peak and possible reasons are less phase transition at this spot or even different phase transition or errors during measurement, when focusing on the scratching center - even though the Raman response volume is in the scratch depth range, a wrong focus can hinder or prevent the measurement of a phase in the spot - or overlapping.



(a)



(b)

Figure 5.4: (a) Overview Berkovich 0 scratch spectrums - each color represents measurements at the one different cutting depth. Zoom in for experiments represented in blue color in (b) Overview scratch Berkovich 0 for cutting depth = 0.8 - absence of Si-IV peaks

It can be seen from Table 5.2 that the Raman intensity ratio decreases slightly with increasing residual depth. This was expected and agrees with Gogotsi et al. who show that amorphous silicon is formed at a small depth of cut while at larger depth of cut Si-IV is formed. This means that with increasing depth of cut, more hexagonal diamond crystalline silicon is formed leading to a smaller ratio of amorphous against crystalline phase. Figure 5.5 plots the data from Table 5.2, to get a better visualization of the decrease in intensity ratio with increasing cutting depth. One can see that for scratches performed with Vickers 45° reveal a different behavior: the ratio increases with increasing cutting depth. A possible reason for this behavior is the more brittle fracture present in face-first experiments, leading to less phase transition and, therefore, less Si-IV being produced. Furthermore, Vickers 0° scratches show an increase in intensity ratio followed by a drop, possibly due to less phase transformed at the measurement point or overlapping with undisturbed surface of the first data.

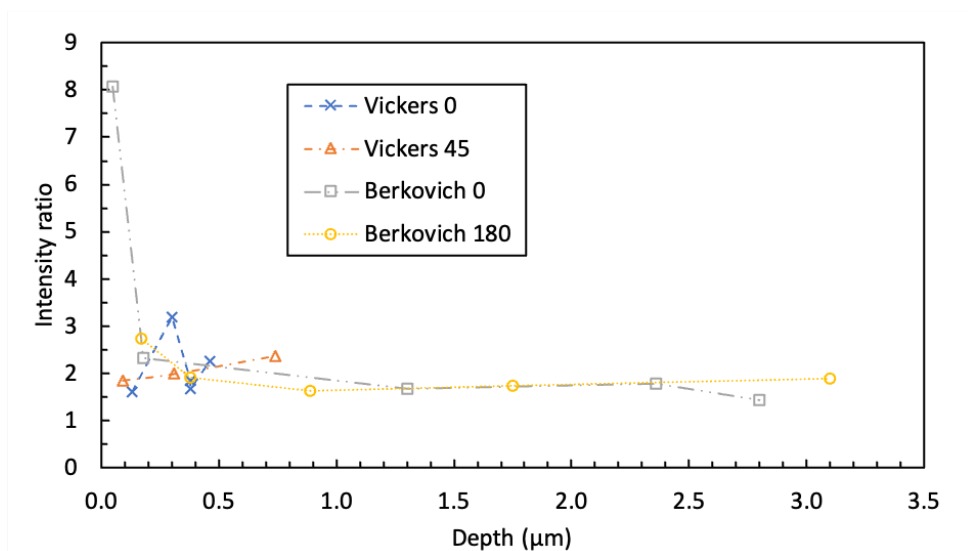


Figure 5.5: Intensity ratio vs cutting depth for all scratch experiments

Observing scratch numbers 308 5, 315 6 and 310 3 (Vickers 0 and Berkovich 180 degrees, respectively), which exhibit the same residual depth, it is possible to see that changing the indenter doesn't influence the intensity of amorphous silicon produced. The same happens when it comes to changing of orientation within one indenter shape - scratches 313 4 and 310 4 (Vickers 0 and 45 degrees, respectively), show similar residual depth and intensity ratio. Shimimaka et al. [36] demonstrated that edge-on scratches results in brittle fracture while face-on performed ductile mechanism, due to the highly localized stress acting along the edge. The experiments demonstrate that for the same residual depth, both edge and face-on scratches can lead to a ductile machine, resulting in a phase transition and amorphization of silicon, as mentioned above. Considering the diamond wire sawing process, the results obtained in this research indicates that although the stress is sufficiently high for phase transitions, the grain shape of the diamonds in the wire does not influence the residual phase on the cut silicon surface or the ratio between amorphous and crystalline phase produced - considering that the grains are sharp and not blunt, as Rockwell scratches have only caused brittle fracture and cracks and no material removal. Furthermore, the decrease on intensity ratio with increasing cutting depth demonstrate that more amorphous phase is produced at smaller cutting depths, which can be controlled by the feed speed during the process. Another important aspect to be pointed out is that while Si-IV and Si-I have the same density, a-Si has a lower atomic density, leading to a volumetric expansion of 3-10% when Si-I is transformed to a-Si. The importance of knowing the amorphization intensity - described by the amount of a-Si formed in comparison to other crystalline phases - and to identify which phase transitions occurs during silicon

Indenter	Angle	Scratch ID	Residual depth μm	Raman ratio
Vickers	0	315_5	0.13	1.61
		308_4	0.3	3.18
		308_5	0.38	1.85
		315_6	0.38	1.67
		308_6	0.46	2.25
	45	322_2	0.09	1.85
		322_4	0.31	1.99
		322_6	0.74	2.37
	Berkovich	0	313_3	0.05
313_4			0.18	2.33
313_5			1.3	1.68
309_1			2.36	1.78
309_3			2.8	1.44
180		310_4	0.17	2.74
		310_3	0.38	1.90
		310_5	0.89	1.63
		321_3	1.75	1.74
		321_5	3.1	1.88

Table 5.2: Raman intensity ratio and depth of cut

machining is that different phases have different intensities, as described in Section 2.2.2 therefore, thin wafers can bend with density change.

Conclusion and Future Work

6.1 Conclusion

Experiments were conducted to investigate the influence of the diamond grain shape and orientation on the residual phases during scratching of silicon at high scratching speeds (closer to the cutting speed used at sawing industry), which have not much detailed studies about it. Three different indenter shape with two different orientations were used to perform the investigation.

To have a quantitative parameter, the Raman intensity ratio was calculate for each scratch, considering the amorphous and Si-IV peaks. In total, 110 data points were obtained by performing measurements using Raman microscope, 7 scratch series, 3 scratches per serie and 5 measurements per scratch. The scratch depth or residual depth of cut was obtained with Sensofar microscopy, with an overview image of the scratch series and using the profile height difference tool available in the software. Also, a qualitatively analysis on the scratch morphology, to characterize it either as ductile or brittle removal mode. After the analysis, it was possible to conclude:

- 1 - Blunt tools does not perform material removal on the surface, only brittle fracture with micro-cracks;
- 2 - Experiments conducted with edge-first orientation (0°) show less brittle fracture when compared to face-first, for the same scratch depth;
- 3 - Besides the different morphology, changing the orientation does not influence the residual phase of the silicon surface - Raman spectrums for both orientations exhibit mostly the same phases. The same happens to different sharp indenter shape - the residual phases are mostly the same;
- 4 - The Raman intensity ratio is a parameter which describes and quantify the relative significance between two phases, in this case Si-IV and a-Si, in order to give an estimation for the amount of each phase present. It was shown that for higher cutting depths, this ratio is smaller, which means that less amorphous silicon is produced. But no influence was found on the different indenters or orientations on the ratio - the amount of phase produced was not controlled by these changes.

This has an significant importance for the diamond wire sawing technique because it means that the

phase transitions occurred after sawing, while the wire diamonds are still sharp, cannot be attributed to the change of the shape and wear of the diamonds. Thus it is necessary to have further investigations on this topic. Finally, it is important to highlight that from the repetitions, it was possible to see that the Raman intensity ratio is very sensitive to the position where the analysis is made, but can still be used with dedicated attention.

6.2 Future Work

In this thesis, a method to study the influence of the grain shape on the residual phases of the silicon surface and shown no significant influence on the diamond shape was presented. Considering that after sawing, the wafer can show different phases within the length, it is important to conduct further investigation on where this comes from.

The next steps for continuing this research should be to include to the evaluation the force measurements: evaluate the forces and pressure at the spots were the phases were determined, considering that different phases are produced in specifics pressures.

Furthermore, a code is already in development for analyze the force and pressure at the ductile-to-brittle (dtb) transition, considering the length, time and position of the scratch. The Raman measurement at the dtb transition was not possible due to limitations on the microscope table and size of the workpiece. It would be interesting to find a solution for this limitation and analyze phase transitions at dtb position.

In linking with the process, a comparison with sawn wafers and the phases found on these workpieces. An analysis on the Raman intensity ratio on some wafers has already been performed.

Appendix

A.1 Scratches profiles

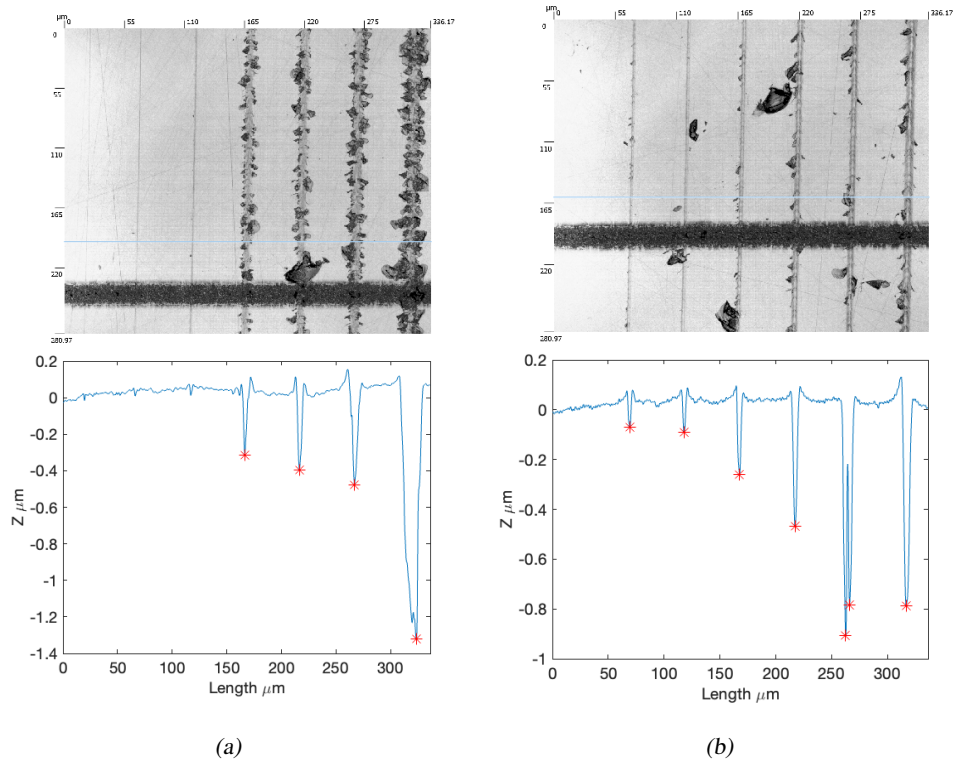


Figure A.1: Overview and profile of Vickers (a) 0 and (b) 45 degrees scratches

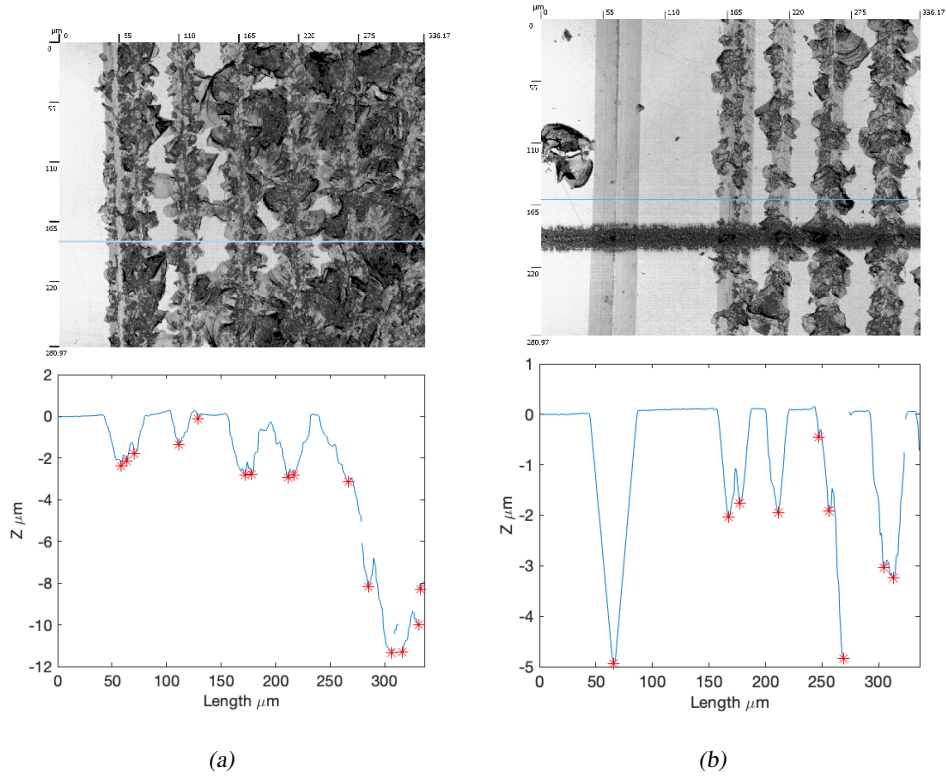


Figure A.2: Overview and profile of Berkovich (a) 0 and (b) 180 degrees scratches

A.2 Groove center Raman overview

The following images are the Raman data overview for each indenter and orientation set. Each color of the spectrum is one residual depth of cut and its respective repetitions.

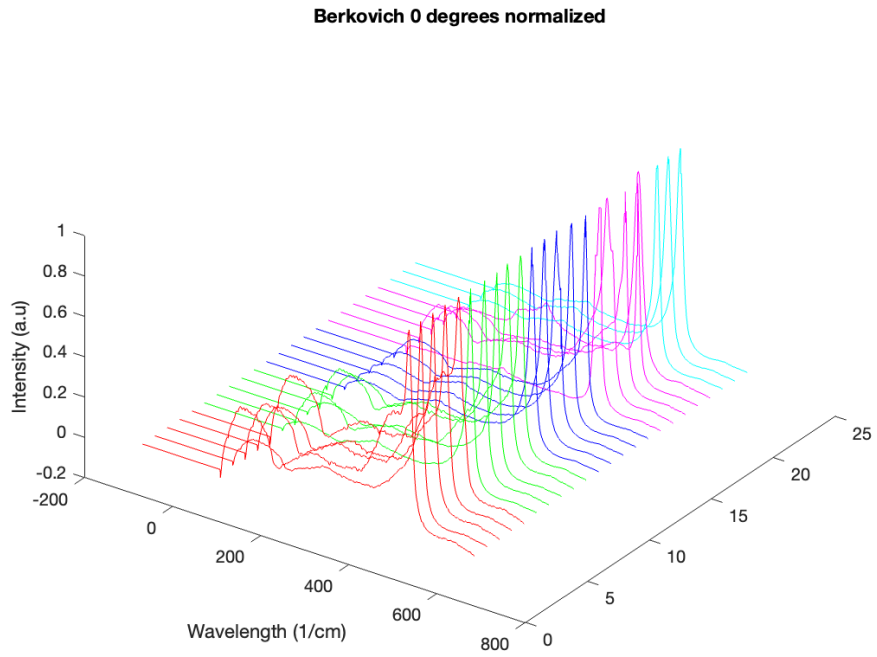


Figure A.3: Raman data analysis overview for berkovich edge-on scratches

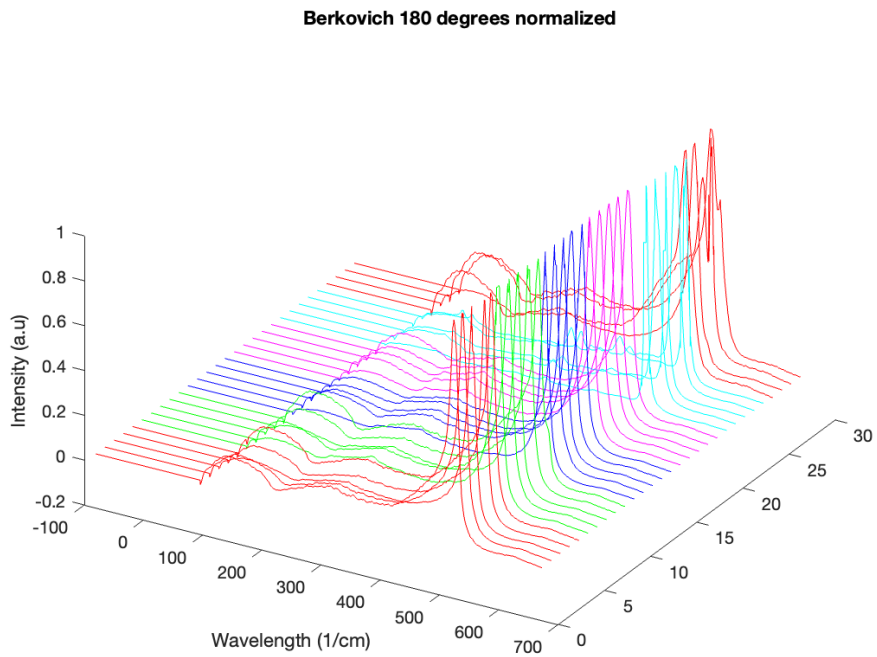


Figure A.4: Raman data analysis overview for berkovich face-on scratches

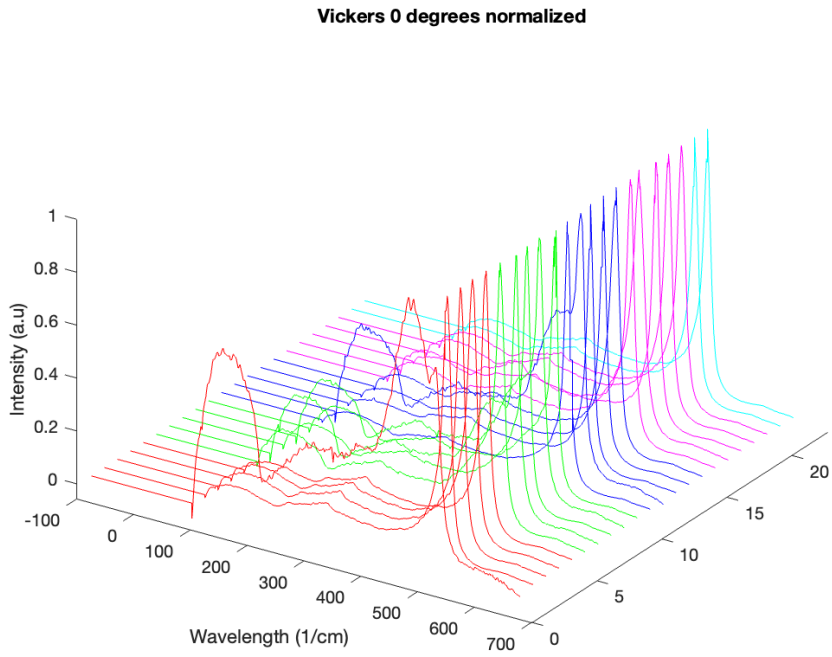


Figure A.5: Raman data analysis overview for vickers edge-on scratches

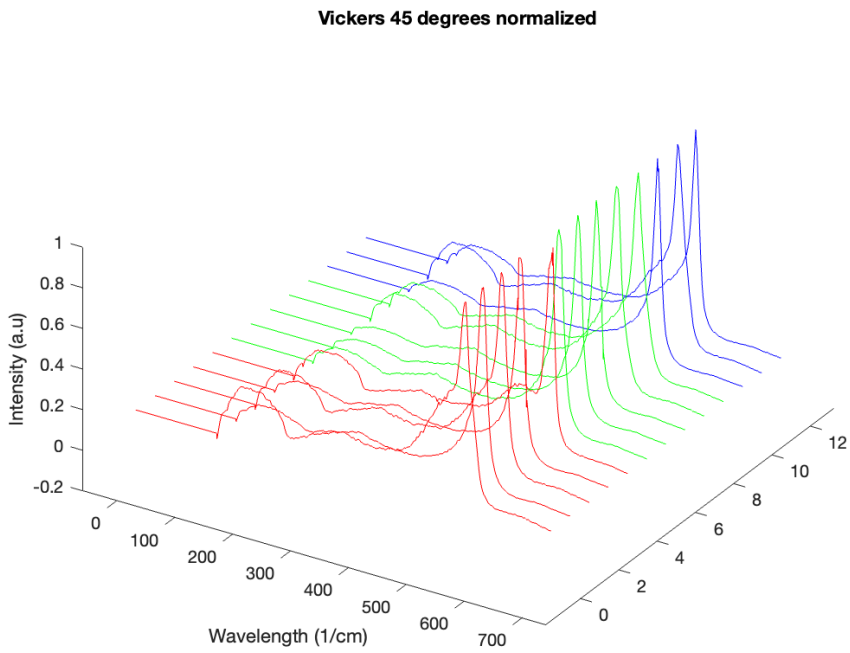


Figure A.6: Raman data analysis overview for vickers face-on scratches

Bibliography

- [1] A. Kumar and S.N. Melkote. “Diamond Wire Sawing of Solar Silicon Wafers: A Sustainable Manufacturing Alternative to Loose Abrasive Slurry Sawing”. In: *Procedia Manufacturing* 21 (2018). 15th Global Conference on Sustainable Manufacturing, pp. 549–566.
- [2] Global market outlook, ed. *Report of European photovoltaic industry association*. 2012.
- [3] Navigant Research, ed. *Report Navigant Consulting Solar PV market forecast*; 2012.
- [4] H-J. Möller. *Chapter 18 - Wafer processing*. Ed. by P. Rudolph. Elsevier, 2015.
- [5] “Chapter 12.- Wafer cleaning, etching and texturization”. In: *Handbook of Photovoltaic Silicon*. Ed. by D. Yang. Springer, 2019.
- [6] W.C O’Mara, R.B Herring, and L.P Hunt. INSPEC, 2009.
- [7] A. Bidiville. “Wafer sawing processes: from microscopic phenomena to macroscopic properties”. PhD thesis. 2010.
- [8] B. El-Kareh and L.N Hutter. *Silicon Analog Components*. 2015.
- [9] N. Maluf. *An Introduction to Microelectromechanical Systems Engineering*. Artech House, Inc, 2002.
- [10] M. Tilli. “Chapter 4 - Silicon Wafers: Preparation and Properties”. In: *Handbook of Silicon Based MEMS Materials and Technologies (Second Edition)*. Ed. by M. Tilli et al. Second Edition. Micro and Nano Technologies. Boston: William Andrew Publishing, 2015, pp. 86–103.
- [11] R. Hull, ed. *Properties of crystalline silicon*. 1999.
- [12] D.R Evans. *Crystal structure and growth - Microelectronic Device Fabrication 1*. Lecture notes. Portland State University - USA, 2014.
- [13] M. Tilli and A. Haapalinna. “Chapter 1 - Properties of Silicon”. In: *Handbook of Silicon Based MEMS Materials and Technologies (Second Edition)*. Ed. by M. Tilli et al. Second Edition. Micro and Nano Technologies. Boston: William Andrew Publishing, 2015, pp. 3–17.
- [14] P.A.N Bernardini. *Análise de Falhas em materiais vol 1*. Lecture notes. Universidade Federal de Santa Catarina, 2020.

- [15] G. Bifano, A. Dow, and O. Scattergood. “Ductile-regime grinding of brittle materials: Experimental results and the development of a model”. In: *Advances in Fabrication and Metrology for Optics and Large Optics* (1989).
- [16] W. Huang et al. “A predictive model of critical depth of cut for ultrasonic elliptical vibration cutting of brittle materials”. In: *9th International Symposium on Advanced Optical Manufacturing and Testing Technologies: Advanced Optical Manufacturing Technologies*. Ed. by Xiong Li et al. Vol. 10838. International Society for Optics and Photonics. SPIE, 2019, pp. 82–91.
- [17] K. Afa and P. Capper. Springer US, 2013.
- [18] T. Juliano, V. Domnich, and Y. Gogotsi. “Phase transformations under dynamic loading”. In: *High-Pressure Surface Science and Engineering*. 2004, p. 20. ISBN: 9780429144097.
- [19] P. Pirouz et al. “The martensitic transformation in silicon—I experimental observations”. In: *Acta Metallurgica et Materialia* 38.2 (1990), pp. 313–322.
- [20] V. Domnich and Y Gogotsi. “Phase Transformations in Silicon Under Contact Loading”. In: *Rev. Adv. Mater. Sci.* 3 (Jan. 2002).
- [21] M. Ganchenkova and R.M Nieminen. “Chapter 9 - Mechanical Properties of Silicon Microstructures”. In: *Handbook of Silicon Based MEMS Materials and Technologies (Second Edition)*. Ed. by Markku Tilli et al. Second Edition. Micro and Nano Technologies. William Andrew Publishing, 2015, pp. 253–293.
- [22] L.C. Zhang and W.C.D. Cheong. “Molecular dynamics simulation of phase transformations in monocrystalline silicon”. In: *High-Pressure Surface Science and Engineering*. 2004, p. 63. ISBN: 9780429144097.
- [23] Pirouz. P. et al. “The martensitic transformation in silicon—III. comparison with other work”. In: *Acta Metallurgica et Materialia* 38.2 (1990), pp. 329–336.
- [24] U. Dahmen et al. “The martensitic transformation in silicon—II. crystallographic analysis”. In: *Acta Metallurgica et Materialia* 38.2 (1990), pp. 323–328.
- [25] J.F. Cannon. “Behavior of the Elements at High Pressures”. In: *Journal of Physical and Chemical Reference Data* 3 (1974).
- [26] S. Gao et al. “Warping of silicon wafers subjected to back-grinding process”. In: *Precision Engineering* 40 (2015), pp. 87–93.
- [27] H.G.M. Lewis I.R. and Edwards, ed. *Handbook of Raman spectroscopy*. Ed. by INC Marcel Dekker.
- [28] V. Domnich and Y. Gogotsi. “Raman microspectroscopy”. In: *High-Pressure Surface Science and Engineering*. 2004, p. 17.
- [29] “Raman Instrumentation”. In: *Practical Raman Spectroscopy – An Introduction*. John Wiley & Sons, Ltd, 2013. Chap. 4, pp. 61–100.
- [30] Z. Xu et al. “Topic Review: Application of Raman Spectroscopy Characterization in Micro/Nano-Machining”. In: *Micromachines* 9.7 (2018).
- [31] Jiwang Y., Tooru A., and Tsunemoto K. “Nondestructive measurement of machining-induced amorphous layers in single-crystal silicon by laser micro-Raman spectroscopy”. In: *Precision Engineering* 32.3 (2008), pp. 186–195.
- [32] Y. Gogotsi et al. “Raman microspectroscopy analysis of pressure-induced metallization in scratching of silicon”. In: *Semiconductor Science and Technology* 16 (2001), pp. 345–352.

- [33] Y. Gogotsi, C. Baek, and F. Kirscht. “Raman microspectroscopy study of processing-induced phase transformations and residual stress in silicon”. In: *Semiconductor Science and Technology* 14.10 (Sept. 1999), pp. 936–944.
- [34] B. Wang et al. “Effect of scratching speed on phase transformations in high-speed scratching of monocrystalline silicon”. In: *Materials Science and Engineering: A* 772 (2020), p. 138836.
- [35] R. Gassilloud et al. “Deformation mechanisms of silicon during nanoscratching”. In: *physica status solidi (a)* 202.15 (2005), pp. 2858–2869.
- [36] O. Shikimaka and P. Prisacaru. “Deformation mechanisms under nanoscratching of Si: effect of scratching speed, load and indenter orientation”. In: *Materials Research Express* 6.8 (May 2019), p. 085011.

